Smart Materials and Structures

PAPER • **OPEN ACCESS**

Modeling of elastic, electromechanical coupling and damping nonlinearities for cantilever beam piezoelectric energy harvesters

To cite this article: Radhika Choudhary *et al* 2026 *Smart Mater. Struct.* **35** 015028

IOP Publishing Smart Mater. Struct. **35** (2026) 015028 https://doi.org/10.1088/1361-665X/ae2cd0

Smart Materials and Structures

Modeling of elastic, electromechanical coupling and damping nonlinearities for cantilever beam piezoelectric energy harvesters

Check for updates

OPEN ACCESS

RECEIVED
30 August 2025

REVISED
25 November 2025

ACCEPTED FOR PUBLICATION
15 December 2025

PUBLISHED
6 January 2026

Radhika Choudhary[1,*], **Imen Rzig**[1], **Edith Roland Fotsing**[1], **Annie Ross**[1] **and Guilhem Michon**[2]

[1] Laboratoire d'Analyse Vibratoire et Acoustique (LAVA), Department of Mechanical Engineering, École Polytechnique de Montréal, PO Box 6079, Station Centre-Ville, Montréal, Québec H3C 3A7, Canada

[2] ICA, Université de Toulouse, CNRS, ISAE-Supaero, MINES ALBI, UT3, INSA, Toulouse 31055, France

[*] Author to whom any correspondence should be addressed.

E-mail: radhika.choudhary@etud.polymtl.ca

Keywords: piezoelectric, energy harvesting, nonlinearity, nonlinear damping, dielectric loss

Abstract

Piezoelectric energy harvesters (PEHs) exhibit nonlinear behavior due to the inherent nonlinear properties of piezoelectric materials and display a highly damped response. In this article, we experimentally and analytically investigate the material and damping nonlinearities of cantilever beam PEHs. A nonlinear model for piezoelectric cantilever is introduced, incorporating higher-order elastic nonlinearities, electromechanical coupling nonlinearities and nonlinear damping. The nonlinear damping is attributed to structural dissipation, electromechanical conversion and dielectric losses. The method of multiple scales is employed to derive an analytical solution for the nonlinear governing equations, which facilitates the calculation of material nonlinearity coefficients and damping parameters through curve-fitting methods. The model shows good agreement with experimental results and is subsequently used to study PEH performance over a wide range of load resistances and base acceleration levels, revealing that material nonlinearity and damping parameters critically influence the optimal load resistance and resonance frequency of the piezoelectric cantilever.

Nomenclature

$\dot{()}$	First derivative with respect to time t
$\ddot{()}$	Second derivative with respect to time t
$()'$	First derivative with respect to axial coordinate x
$()''$	Second derivative with respect to axial coordinate x
A_p	Cross-section area of piezoelectric layer
A_s	Cross-section area of substrate layer
B	Coeff. of governing equations representing linear structural dissipation parameter
b_p	Width of piezoelectric layer
b_s	Width of substrate layer
C	Coeff. of governing equations representing capacitance
C_{eq}	Capacitance per unit length
c.c.	Complex conjugate
D_k	First partial derivative with respect to time scale T_k
d_{31}	Piezoelectric constant
$G_{m,k}$	Coeff. of governing equations representing nonlinear structural dissipation parameters
h_{pc}	Distance of the center of piezoelectric layer to the neutral axis
$I_{p,k}$	k^{th} moment of area for piezoelectric layer
$I_{s,k}$	k^{th} moment of area for substrate layer
L	Length of cantilever beam
$N_{e,k}$	Coeff. of governing equations representing electromechanical coupling nonlinearity
$N_{m,k}$	Coeff. of governing equations representing elastic nonlinearity
P	Generalized vibration response function
p	Generalized vibration response amplitude

p_{peak}	Peak value of the generalized vibration response amplitude p
Q	Voltage response function
R	Load resistance
T_k	Time scale of order k
t	Time
t_{p}	Thickness of piezoelectric layer
t_{s}	Thickness of substrate layer
V	Voltage
v	Transverse displacement
$\ddot{v}_{\text{b}}$	Base acceleration
x	Axial coordinate
Y_{p}	Elasticity modulus of piezoelectric material
Y_{s}	Elasticity modulus of substrate material
y	Transverse coordinate
Z	Complex-value electromechanical conversion factor
Φ	Coeff. of governing equations representing dielectric dissipation parameter
$\mathcal{W}_{\text{nc}}$	Nonconservative virtual work
Γ	Coeff. of governing equations representing normalized effective mass contributing to the forcing term
Θ	Coeff. of governing equations representing electromechanical coupling
Λ	Coeff. of governing equations representing electromechanical conversion dissipation parameter
Ω	Excitation frequency
α_k	Elastic nonlinearity coefficient of piezoelectric material
β_k	Electromechanical coupling nonlinearity coefficient of piezoelectric material
ε	Small bookkeeping parameter for perturbation analysis
ζ_r	Damping ratio
η_r	Generalized time-dependent displacements
ρ_{p}	Density of piezoelectric material
ρ_{s}	Density of substrate material
ψ	Argument of the complex-valued generalized vibration response function P
ω	Frequency
ω_{oc}	Open-circuit resonance frequency
ω_{r}	Natural frequency
ω_{sc}	Short-circuit resonance frequency
$\Delta\omega_{\text{em}}$	Electromechanical resonance frequency shift
$\Delta\omega_{\text{nl}}$	Nonlinear resonance frequency shift
ϵ_{33}	Piezoelectric permittivity
ϑ	Coupling factor
ϕ_r	Normalized mode shape function

1. Introduction

Piezoelectric energy harvesters (PEH) convert ambient vibrations in buildings, machinery, vehicles, aircraft, etc, into useful electrical energy. This process provides alternative energy to electronic devices while also attenuating vibrations in the system. PEHs are based on the direct piezoelectric effect and convert mechanical strain energy to electrical energy. The most used configurations of PEH are unimorph and bimorph. The unimorph configuration consists of one substrate layer and one piezoelectric layer. In the bimorph configuration, two piezoelectric layers are there on either side of the substrate layer. The piezoelectric layers in bimorph can be connected in series or parallel.

Most studies available in the literature for PEH performance optimization consider linear behavior, which is valid at low acceleration levels [1–10]. However, piezoelectric materials exhibit nonlinear behavior at high strain levels [11–14]. A number of models for nonlinear piezoelectric systems are based on the piezoelectric microcantilever sensor model [15–17], which includes material, geometric and inertia nonlinearities. Among these, material nonlinearities can be classified into elastic, electromechanical coupling, and electric field nonlinearities, with elastic nonlinearity typically being the most significant contributor to the piezoelectric system behavior [16, 18–20].

Several researchers have modeled PEHs using second-order material nonlinearities while utilizing fixed damping. Patel *et al* [21] included second-order material nonlinearities in the model for unimorph PEH while also accounting for substrate material nonlinearity. Salmani and Rahimi [22] developed a model including second-order nonlinearities for an exponentially tapered unimorph PEH, showing that output voltage decreases as the tapered beam tip becomes narrower. In thin cantilever beams, higher-order nonlinearities are often present due to increased strain and electric field, making second-order nonlinearity insufficient to model the behavior. Additionally, these studies assumed constant damping, which fails to account for the increased dissipation observed at higher strain levels, thus limiting their accuracy.

A few researchers have addressed higher-order material nonlinearities and nonlinear damping for PEH. Stanton *et al* [23, 24] attributed nonlinear damping to energy dissipation arising from nonconservative work in their analysis of a bimorph PEH with a tip mass, revealing that elastic nonlinearities become significant up to the fifth-order at higher acceleration levels, and nonlinear damping plays a critical role. Abdelkefi *et al* [25, 26] investigated quadratic damping and cubic material nonlinearities for unimorph PEH with tip mass, showing that accurate voltage predictions required incorporating at least three modes in the model. Leadenham and Erturk [27] investigated the nonlinear dynamic behavior of soft bimorph piezoelectric cantilevers (e.g. PZT) for sensing, actuation and energy harvesting applications. Their study incorporated second-order nonlinear structural dissipation, demonstrating increased damping as base acceleration increased. Yang and Upadrashta [28] also modeled higher-order elastic nonlinearities and second-order nonlinear damping for a cantilever PEH, showing that the influence of nonlinear damping grows with increasing base acceleration. Most of these studies have typically focused on a single load resistance over a limited range of acceleration levels insufficient to induce higher-strain conditions, even though load resistance is recognized as an important parameter for optimizing PEH performance [29–32].

Leadenham and Erturk [33] presented an improved model for bimorph PEH with material and dissipative nonlinearities, implementing it for both resistive and capacitive loads. The model was validated across various acceleration levels and load resistances. They attributed the attenuation of power output near open-circuit to dielectric losses, discussing the effect of base acceleration on peak power frequency. However, the PEH performance was not investigated at higher acceleration levels where large strains and dissipations are present. Lan *et al* [34] studied nonlinear PEHs and derived approximate solutions for optimal resistance, power limits, and critical electromechanical coupling, but did not examine the electromechanical conversion or dielectric losses observed near open-circuit. Machado *et al* [35] presented a unified general method for modeling multimodal energy harvesters with geometric, material, and damping nonlinearities. However, in these works, the effect of load resistance on nonlinear behavior was not clearly investigated, even though it is a key parameter for optimizing PEH performance.

In this work, we are motivated to investigate the impact of elastic and electromechanical coupling nonlinearities, as well as nonlinear damping, on piezoelectric cantilevers, particularly across varying load resistances and under high acceleration levels that induce high-strain conditions. The load resistance is a critical parameter for PEH optimization, and its optimal value is influenced by the nonlinear response of the PEH at different acceleration levels. Therefore, studying nonlinear PEH behavior across load resistance contributes to a better understanding of the energy harvesting mechanism and supports performance optimization over an extended operational range.

We build upon our previously developed unified nonlinear model [36], in which an iterative method was used to calculate damping at each acceleration level using the half-power bandwidth method. This formulation is limited as it does not generalize damping across acceleration levels and load resistances, limiting accuracy. The current study introduces an advanced nonlinear model incorporating nonlinear damping in the governing equations of the PEH system along with the higher-order elastic nonlinearities and electromechanical coupling nonlinearities. This model includes nonlinear structural dissipation and accounts for electromechanical conversion and dielectric losses. By generalizing the nonlinear terms in the governing equations to the n^{th} order, the model is adaptable to any desired level of complexity. The nonlinear equations are solved using the method of multiple scales to derive an analytical solution, which facilitates the identification of nonlinearity coefficients and damping parameters via curve fitting. The proposed model is validated against experimental data and demonstrates a closer agreement as compared to the previous nonlinear models. The proposed model is then employed to enhance our comprehension of the effect of material nonlinearities, nonlinear structural dissipation and dielectric losses on PEH performance across varying load resistance. The PEH output is studied numerically and experimentally for series and parallel bimorph configurations across varying load resistance at various base acceleration values.

2. Methodology

2.1. Nonlinear governing equations of PEH

The PEH comprises a substrate layer covered with piezoelectric layers, as shown in figure 1. The width of the piezoelectric layer, b_{p}, is the same as the width of the substrate layer, b_{s}, and both widths are uniform along the cantilever length, L. The PEH is excited by a base acceleration $\ddot{v}_{\mathrm{b}}(t)$ at its base i.e. at $x = 0$.

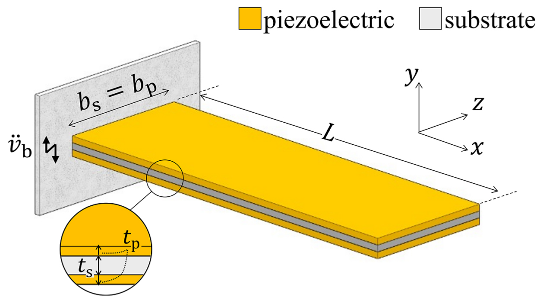

Figure 1. Schematic of the piezoelectric cantilever beam for energy harvesting.

The nonlinear governing equations are derived by modifying the electroelastic enthalpy expression to include higher-order elastic and electromechanical coupling nonlinear terms leading to nonlinear constitutive equations, which are generalized for n^{th} order of nonlinearity. The extended Hamilton's principle is utilized to derive the governing nonlinear equations from the energy expression of the cantilever as described in [36]. Using linear proportional damping ζ_r, the modal equation of motion for the nonlinear PEH and the circuit equation are given as

$$\ddot{\eta}_r + 2\zeta_r\omega_r\dot{\eta}_r + \omega_r^2\eta_r + \sum_{k=1}^{n-1} N_{\mathrm{m},k}\eta_r^{k+1} - \Theta V - \sum_{k=1}^{n-1} N_{\mathrm{e},k}\eta_r^{k} V = \Gamma\ddot{v}_{\mathrm{b}} \tag{1}$$

$$\dot{V} + \Theta\dot{\eta}_r + \sum_{k=1}^{n-1} N_{\mathrm{e},k}\eta_r^{k}\dot{\eta}_r + \frac{V}{R} = 0. \tag{2}$$

Here η_r are the generalized time-dependent displacement, and V is the voltage generated in the PEH. The coefficients $N_{\mathrm{m},k}$ represent the elastic nonlinearity of piezoelectric material and $N_{\mathrm{e},k}$ represent the electromechanical coupling nonlinearity. Further, C, Θ and Γ are the capacitance, electromechanical coupling and normalized effective mass contributing to the forcing term, respectively. These coefficients are expressed below

$$\Theta = \int_0^L -2Y_{\mathrm{p}}d_{31}\vartheta b_{\mathrm{p}}h_{\mathrm{pc}}\phi_r''\mathrm{d}x \tag{3}$$

$$\Gamma = \int_0^L \left(\rho_{\mathrm{s}}b_{\mathrm{s}}t_{\mathrm{s}} + \rho_{\mathrm{p}}b_{\mathrm{p}}t_{\mathrm{p}}\right)\phi_r\mathrm{d}x \tag{4}$$

$$C = \int_0^L C_{\mathrm{eq}}\mathrm{d}x \tag{5}$$

$$N_{\mathrm{m},k} = \int_0^L \frac{(k+2)}{2}(-1)^{k+2}\alpha_k I_{\mathrm{p},k+2}(\phi_r'')^{k+2}\mathrm{d}x \quad k = 1,2,3\ldots, n-1 \tag{6}$$

$$N_{\mathrm{e},k} = -\int_0^L \frac{k+2}{2}(-1)^{k+1}\left(\frac{\vartheta\beta_k I_{\mathrm{p},k+1}}{t_{\mathrm{p}}}\right)(\phi_r'')^{k+1}\mathrm{d}x \quad k = 1,2,3\ldots, n-1 \tag{7}$$

where ϕ_r are normalized mode shape functions. The tip displacement is expressed as $v(t) = \sum_{r=1}^{\infty}\phi_r(x)\eta_r(t)$.

In the above equations, the geometric nonlinearity effects are neglected because it becomes significant at much higher accelerations than those considered in our study.

The area moments are calculated as $I_{\mathrm{s},k} = \iint_{A_\mathrm{s}} y^k \mathrm{d}A$ and $I_{\mathrm{p},k} = \iint_{A_\mathrm{p}} y^k \mathrm{d}A$. The electromechanical coupling factor is $\vartheta = 1$ for unimorph PEH, $\vartheta = 0.5$ for bimorph-series PEH, and $\vartheta = 1$ for bimorph-parallel PEH. The coupling factor is reduced by half in bimorph-series PEH since the voltage is measured across both piezoelectric layers. The equivalent capacitance per unit length is $C_\mathrm{eq} = \frac{b_\mathrm{p}\epsilon_{33}}{t_\mathrm{p}}$ for unimorph PEH, $C_\mathrm{eq} = \frac{b_\mathrm{p}\epsilon_{33}}{2t_\mathrm{p}}$ for bimorph-series PEH and $C_\mathrm{eq} = \frac{2b_\mathrm{p}\epsilon_{33}}{t_\mathrm{p}}$ for bimorph-parallel PEH. The description of the variables used in these equations is given in Nomenclature.

We employ the nonconservative virtual work formulation provided in [24], which consists of linear and nonlinear structural dissipation, electromechanical conversion losses and dielectric losses. To extend the model, we generalize the nonlinear structural dissipation to the n^th order and write the virtual work as

$$\delta \mathcal{W}_\mathrm{nc} = -\left(B\dot{\eta}_r + \sum_{k=1}^{n-1} G_{\mathrm{m},k}\eta_r^k\dot{\eta}_r - \Lambda\dot{V}\right)\delta\eta + \left(\Lambda\dot{\eta}_r + \Phi\dot{V}\right)\delta V \tag{8}$$

where B is the linear structural dissipation parameter, $G_{\mathrm{m},k}$ are the nonlinear structural dissipation parameters, Λ is the electromechanical conversion dissipation parameter, and Φ is the dielectric dissipation parameter.

After implementing the extended Hamilton principle, we obtain the governing nonlinear equations as given below

$$\ddot{\eta}_r + B\dot{\eta}_r + \sum_{k=1}^{n-1} G_{\mathrm{m},k}\eta_r^k\dot{\eta}_r - \Lambda\dot{V} + \omega_r^2\eta_r + \sum_{k=1}^{n-1} N_{\mathrm{m},k}\eta_r^{k+1} - \Theta V - \sum_{k=1}^{n-1} N_{\mathrm{e},k}\eta_r^k V = \Gamma\ddot{v}_\mathrm{b} \tag{9}$$

$$C\dot{V} + \Theta\dot{\eta}_r + \sum_{k=1}^{n-1} N_{\mathrm{e},k}\eta_r^k\dot{\eta}_r + \frac{V}{R} + \Lambda\ddot{\eta}_r + \Phi\ddot{V} = 0. \tag{10}$$

2.2. Analytical solution

The coupled nonlinear equations are solved using the method of multiple scales, which was implemented previously by researchers [22, 37–40]. The base acceleration $\ddot{v}_\mathrm{b}(t)$ is expressed as $|\ddot{v}_\mathrm{b}|\cos(\Omega t)$, where Ω is the excitation frequency and $|\ddot{v}_\mathrm{b}|$ is the acceleration amplitude. A frequency-detuning parameter σ is introduced, which relates the excitation frequency Ω to the first natural frequency ω_1 of the beam as $\Omega = \omega_1 + \varepsilon^2\sigma$. In other words, the frequency-detuning parameter quantifies the amount of perturbation in the system relative to its natural frequency. The complete details of the derivation of the analytical solution are given in appendix.

The nonlinear analytical frequency response function for the PEH is given below

$$\begin{aligned}\sigma = &\frac{1}{\omega_1 p}\left(\frac{\Lambda}{2}\omega_1 Z_\mathrm{Im}p + S_\mathrm{m} - \frac{1}{2}\Theta Z_\mathrm{Re}p - Z_\mathrm{Re}S_\mathrm{e}\right)\\ &\pm\frac{1}{\omega_1 p}\left(\Gamma^2\frac{|\ddot{v}_\mathrm{b}|^2}{4} - \left(\frac{B}{2}\omega_1 p + \omega_1 J_\mathrm{m} - \frac{\Lambda}{2}\omega_1 Z_\mathrm{Re}p - \frac{1}{2}\Theta Z_\mathrm{Im}p - Z_\mathrm{Im}S_\mathrm{e}\right)^2\right)^{\frac{1}{2}}.\end{aligned} \tag{11}$$

In the above expressions, the subscripts 'Re' and 'Im' correspond to the real and imaginary parts, respectively. The term Z refers to the electromechanical coupling coefficient, defined as $Z = \frac{-i\omega_1\Theta + \omega_1^2\Lambda}{i\omega_1 C + 1/R - \omega_1^2\Phi}$. The variable p denotes the generalized amplitude of vibration, i.e. $p = |\eta|$, which can be computed by numerically solving equation (11) for a specified base acceleration amplitude $|\ddot{v}_b|$. The corresponding tip displacement and output voltage amplitudes are then obtained as $|v| = \phi\,|\eta|$ and $|V| = |Z|\,|\eta|$, respectively. To streamline the otherwise complex expressions, we have introduced the following notation

$$\begin{aligned}S_\mathrm{m} &= \sum_{k\epsilon\mathrm{even}} N_{\mathrm{m},k}\begin{pmatrix}k+1\\k/2\end{pmatrix}\left(\tfrac{p}{2}\right)^{k+1};\ S_\mathrm{e} = \sum_{k\epsilon\mathrm{even}} N_{\mathrm{e},k}\left(\begin{pmatrix}k\\k/2\end{pmatrix} + \begin{pmatrix}k\\k/2-1\end{pmatrix}\right)\left(\tfrac{p}{2}\right)^{k+1}\\ J_\mathrm{m} &= \sum_{k\epsilon\mathrm{even}} G_{\mathrm{m},k}\left(\begin{pmatrix}k\\k/2\end{pmatrix} - \begin{pmatrix}k\\k/2-1\end{pmatrix}\right)\left(\tfrac{p}{2}\right)^{k+1}\end{aligned}. \tag{12}$$

In the above terms, the notation $\begin{pmatrix}[\,]\\[\,]\end{pmatrix}$ is used for binomial coefficient.

Table 1. Material properties and dimensions for the piezoelectric cantilever.

	PZT5H	Brass
Young's modulus (GPa)	66	100
Density (kg m^{-3})	7750	8300
Piezoelectric constant (pm V^{-1})	−298	—
Permittivity (nF m^{-1})	28.8	—
Thickness (mm)	0.127 (each layer)	0.170
Total length (mm)	62.5	
Overhang length (mm)	54.0	
Width (mm)	12.7	

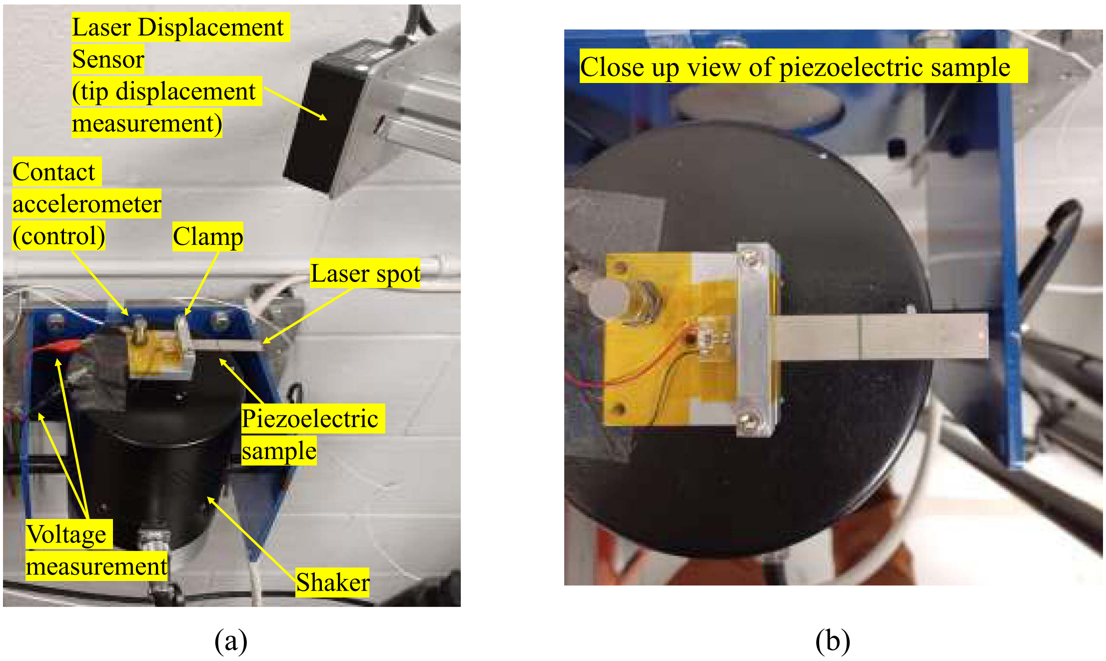

Figure 2. Experimental setup for piezoelectric energy harvester.

2.3. Experimental setup for PEH

This section outlines the experimental procedure for two piezoelectric samples acquired from Piezo.com: a PZT5H bimorph-series cantilever and a PZT5H bimorph-parallel cantilever reinforced with brass substrates. Lead zirconate titanate (PZT) is selected for its superior electromechanical performance and cost-effectiveness. Specifically, the type 5H variant offers a very high piezoelectric strain (charge) constant, making it well-suited for efficient energy conversion. The dimensions and material properties of the samples are detailed in table 1.

The experimental setup, depicted in figure 2, involves clamping the sample to a custom fixture on a TMS 440 N shaker. A contact accelerometer manages the clamp's base acceleration, interfaced with a Spider 81B data acquisition and control system. The sample's electrodes connect to this system through a BNC connector. A Keyence LK-G142 laser displacement sensor measures the beam tip's displacement.

Frequency sweeps are conducted on the piezoelectric samples at various base acceleration levels, ranging from 0.002 g to 1.0 g. The frequency sweep is conducted over a range of 60–75 Hz at a constant rate of 0.1 Hz s^{-1}. Measurements are recorded at a sampling frequency of 20 480 Hz. At each acceleration level, the displacement and voltage frequency responses are measured. These tests are repeated for various load resistances ranging from 0 Ω to 10 MΩ. The values of acceleration levels and load resistances used in the experiments are provided in table 2. The experimental frequency response of the PEH at a 10 MΩ load resistance is examined in section 3.3, where it is compared with the predictions of the nonlinear model.

During post-processing, the peak amplitude of tip displacement and voltage frequency response and the corresponding nonlinear resonance frequency are identified for curve-fitting and experimental comparison.

Table 2. Base acceleration levels and load resistances for experiments.

Base acceleration (g)	0.002, 0.006, 0.01, 0.02, 0.04, 0.06, 0.08, 0.1, 0.2, 0.3, 0.4, 0.5, 0.6, 0.7, 0.8, 0.9, 1.0
Load resistance (Ω)	0, 10, 100, 1 k, 5.1 k, 10 k, 32 k, 99 k, 215 k, 1 M, 10 M

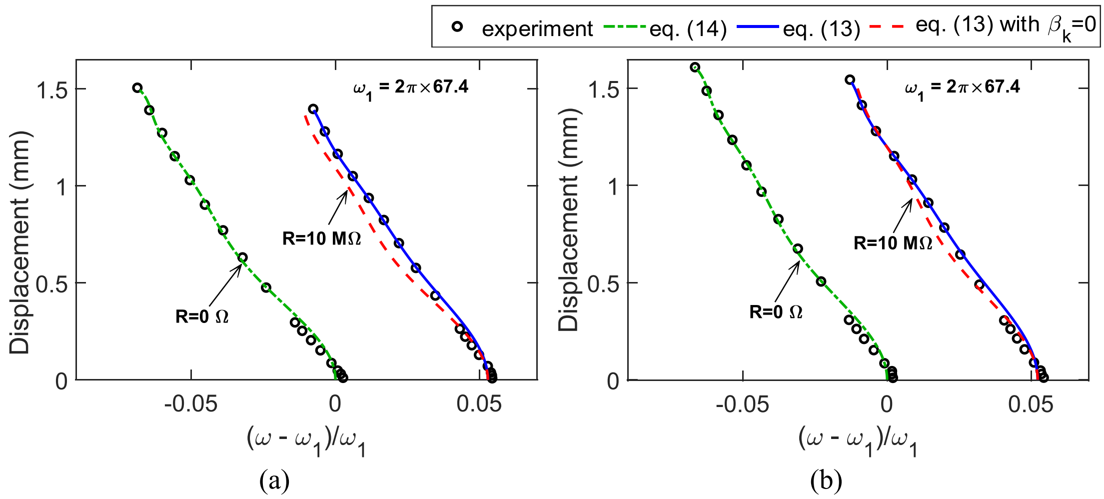

Figure 3. Experimental backbone curves and numerical curve fit: (a) PZT5H series (b) PZT5H parallel.

3. Results and discussion

3.1. Calculation of nonlinearity coefficients for PZT5H samples

The second part of the equation (11) becomes zero at resonance, so σ simply represents the difference between resonance frequency ω and first natural frequency ω_1, i.e. $\sigma = \omega - \omega_1$. The peak value of the generalized vibration response amplitude p at resonance is denoted as p_{peak}. The relationship between resonance frequency (ω) and peak tip displacement ($|v|_{\text{peak}} = \phi_{x=L} p_{\text{peak}}$) represents the backbone curve, i.e. the curve tracing the peaks of the displacement frequency response at various acceleration levels. The backbone curve is analytically formulated from the first part of the equation (11) as

$$\frac{\omega - \omega_1}{\omega_1} = \frac{1}{\omega_1^2 p_{\text{peak}}} \left(\frac{\Lambda}{2} \omega_1 Z_{\text{Im}} p_{\text{peak}} + S_{\text{m}} - \frac{1}{2} \Theta Z_{\text{Re}} p_{\text{peak}} - Z_{\text{Re}} S_{\text{e}} \right). \tag{13}$$

The electromechanical components of equation (13) become zero in the short-circuit condition and the remaining equation is expressed as

$$\frac{\omega - \omega_1}{\omega_1} = \frac{1}{\omega_1^2 p_{\text{peak}}} (S_{\text{m}}). \tag{14}$$

To calculate the elastic nonlinearity coefficients α_k, we calculate the coefficients $N_{\text{m},k}$ from equation (14) by applying curve fitting to the experimental data collected for short-circuit (0 Ω). Subsequently, α_k are obtained using equation (6), and the values are provided in table 3.

Figures 3(a) and (b) present the experimental backbone curves for the two samples for $R = 0\ \Omega$ and $R = 10\ \text{M}\Omega$. As illustrated, the experimental results under short-circuit conditions show good agreement with the fitted model described by equation (14) for both samples.

The significant softening effect of elastic nonlinearity on PEH output is evident, as the resonance frequency decreases considerably with increasing deformation. This effect is quantified by the nonlinear resonance frequency shift $\Delta\omega_{\text{nl}}$, which is the difference between the nonlinear resonance frequency and the linear resonance frequency observed at the lowest acceleration level. At maximum acceleration level in short-circuit, $\Delta\omega_{\text{nl}}$ is -7.1% and -6.9% of ω_1 ($2\pi \times 67.4$ rad s^{-1}) for PZT5H series and PZT5H parallel, respectively, indicating that the contribution of elastic nonlinearity is critical for accurate modeling, particularly at high strains.

To calculate electromechanical coupling nonlinearity coefficients β_k, we utilize the values of α_k from table 3 and calculate the coefficients $N_{\text{e},k}$ from equation (13) using curve-fitting on the experimental

Table 3. Calculated values of nonlinearity coefficients and damping parameters.

Elastic nonlinearity coefficients (calculated from equation (14))							
	α_2	α_4	α_6	α_8	α_{10}		
PZT5H series	-6.3×10^{17}	2.5×10^{25}	-4.9×10^{32}	4.2×10^{39}	-1.3×10^{46}		
PZT5H parallel	-5.4×10^{17}	1.9×10^{25}	-3.4×10^{32}	2.6×10^{39}	-6.9×10^{45}		
Electromechanical coupling nonlinearity coefficients (calculated from equation (13))							
	β_2	β_4	β_6	β_8	β_{10}		
PZT5H series	-5.7×10^{8}	3.4×10^{16}	-6.6×10^{23}	5.0×10^{30}	-1.1×10^{37}		
PZT5H parallel	-4.0×10^{8}	2.2×10^{16}	-3.8×10^{23}	2.6×10^{30}	-5.9×10^{36}		
Damping parameters (calculated from equations (15) and (16))							
	B	Φ	$G_{m,2}$	$G_{m,4}$	$G_{m,6}$	$G_{m,8}$	$G_{m,10}$
PZT5H series	6.53	-9.9×10^{12}	3.2×10^{11}	-1.7×10^{21}	3.6×10^{30}	-3.3×10^{39}	1.0×10^{48}
PZT5H parallel	6.32	-2.4×10^{11}	2.7×10^{11}	-1.3×10^{21}	2.5×10^{30}	-2.0×10^{39}	5.9×10^{47}

data collected for 10 MΩ load resistance. Subsequently, β_k are calculated using equation (7), and the values of are provided in table 3. The experimental data for both samples closely aligns with the numerically fitted equation (13), as shown in figure 3.

Electromechanical coupling nonlinearity has a stiffening effect on the PEH output, increasing the resonance frequency. However, this effect is less significant than the softening caused by elastic nonlinearity. To illustrate the contribution of β_k, we show the plot of 'equation (13) with $\beta_k = 0$' for 10 MΩ load resistance in figure 3, employing α_k values from table 3 but setting β_k to zero. Elastic nonlinearity lowers the resonance frequency, causing the backbone curve to lean towards the left, whereas electromechanical coupling nonlinearity pushes it towards the right, increasing the frequency. The comparison between the curves of 'equation (13)' and 'equation (13) with $\beta_k = 0$' shows the stiffening effect from β_k, which is relatively minor compared to the effect of α_k. At maximum acceleration level for 10 MΩ, $\Delta\omega_{\mathrm{nl}}$ is -6.2% and -6.7% of ω_1 for PZT5H series and PZT5H parallel, respectively.

Due to the bimorph piezoelectric cantilever's symmetry, only nonlinearities proportional to α_k and β_k with $k\epsilon$even affect the system, with others vanishing. Hence, and β_k are computed solely for even $k\epsilon$even.

For fitting the analytical polynomial equation to the data, the polynomial fitting tool in MATLAB® is used with the linear least squares method. A robust least squares approach based on bisquare weighting is utilized. The estimated parameters exhibit narrow 95% confidence bounds. The confidence bounds lie within $\pm5\%$ for the elastic nonlinearity coefficients (α_k), $\pm6\%$ for the electromechanical coupling coefficients (β_k), and $\pm1\%$ for the damping parameters, relative to the values listed in table 3.

Inclusion of higher-order nonlinear terms up to $n = 11$ is required to ensure that the numerically predicted backbone curve lies within the standard deviation of the experimental results. Further details and comparison of the model with experimental data are discussed in our earlier work [36].

To further analyze the reliability of the nonlinearity coefficients presented in table 3, tests were conducted on three samples with identical geometry. The cubic-order nonlinearity coefficients have a percentage deviation of approximately 5% across the three samples. For higher-order nonlinearity coefficients, the percentage deviation is larger across the three samples and it reaches up to 33%. The higher-order nonlinearity coefficients exhibit greater variability across samples and may not be uniquely determined. Nevertheless, the nonlinear resonance frequency of the PEH is relatively less sensitive to such variations. The deviation in nonlinear resonance frequency is only 0.3% for 33% uncertainty in higher-order nonlinearity coefficients.

Another important consideration to note is that the recommended maximum operable strain limit for PZT material is 500 $\mu\varepsilon$ according to the manufacturer (Piezo.com) of our samples. In shaker experiments, the input acceleration oscillates around the target value until it stabilizes. Since the strain in the piezoelectric layer has already reached the value of 415 $\mu\varepsilon$ at an acceleration of 1.0 g, the sample is not subjected to higher acceleration levels in these tests to prevent damage to the sample. For the analytical model developed in this study, the nonlinearity parameters characterized for the piezoelectric material may not be valid for configurations where strain reaches values higher than 415 $\mu\varepsilon$, and a re-characterization using further experimental data may be required.

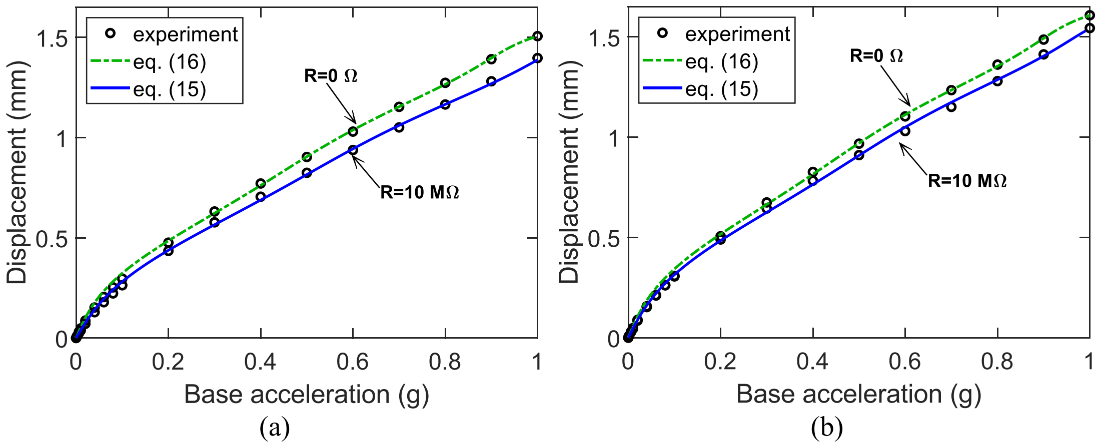

Figure 4. Experimental tip displacement vs. base acceleration and numerical curve fit: (a) PZT5H series (b) PZT5H parallel.

3.2. Calculation of damping parameters for PZT5H samples

The relationship between the peak tip displacement ($|v|_{\text{peak}} = \phi_{x=L} p_{\text{peak}}$) and the base acceleration amplitude ($|\ddot{v}_{\text{b}}|$) is referred to as the displacement curve in this study. The shape of this curve reflects the influence of energy dissipation mechanisms within the PEH and serves as a basis for determining the material loss factors. In the linear regime, tip displacement varies proportionally with base acceleration, and damping remains constant throughout the excitation range. In contrast, for the nonlinear case, this relationship becomes more complex. The analytical expression relating $|\ddot{v}_{\text{b}}|$ to p_{peak} is derived by equating the second part of the RHS of equation (11) to zero as following

$$|\ddot{v}_{\text{b}}| = \frac{2}{\Gamma}\left(\frac{B}{2}\omega_1 p_{\text{peak}} + \omega_1 J_{\text{m}} - \frac{\Lambda}{2}\omega_1 Z_{\text{Re}} p_{\text{peak}} - \frac{1}{2}\Theta Z_{\text{Im}} p_{\text{peak}} - Z_{\text{Im}} S_{\text{e}}\right). \quad (15)$$

In the short-circuit condition, the electromechanical components of equation (15) become zero and the remaining equation is expressed as

$$|\ddot{v}_{\text{b}}| = \frac{2}{\Gamma}\left(\frac{B}{2}\omega_1 p_{\text{peak}} + \omega_1 J_{\text{m}}\right). \quad (16)$$

The linear structural dissipation parameter B and the nonlinear structural dissipation parameters $G_{\text{m},k}$ are calculated from equation (16) via curve-fitting on the experimental data collected for short-circuit. Following this, the dielectric dissipation parameter Φ is determined from equation (15) using curve-fitting on the experimental data collected for 10 MΩ load resistance. The values of B, $G_{\text{m},k}$ and Φ are provided in table 3. We disregard the electromechanical conversion dissipation parameter, assuming its contribution is small compared to the dielectric dissipation. The dielectric loss factor, formulated as $\omega\Phi/C$, is calculated to be 5% for bimorph-series and 3% for bimorph-parallel samples.

Similar to α_k and β_k, the values of $G_{\text{m},k}$ are calculated solely for $k\epsilon$even due to system symmetry.

Figures 4(a) and (b) display the displacement curves (i.e. tip displacement vs. base acceleration) for both samples under $R = 0$ Ω and $R = 10$ MΩ. As illustrated, the experimental data show close agreement with the numerical fits given by equations (15) and (16) for the $R = 10$ MΩ and $R = 0$ Ω cases, respectively.

At accelerations beyond 0.05 g, the tip displacement vs. base acceleration relationship becomes markedly nonlinear, rendering the linear damping assumption invalid. Assuming linear damping leads to significant overshooting of experimental data, highlighting that modeling nonlinear damping is essential at higher acceleration levels for accurate results.

3.3. Comparison with experimental frequency response

Utilizing all material nonlinearity and damping parameters from table 3, we compare the numerical voltage response from equation (11) against experimental data collected for 10 MΩ load resistance, as shown in figure 5. The model accurately predicts the peak voltage magnitude and resonance frequency.

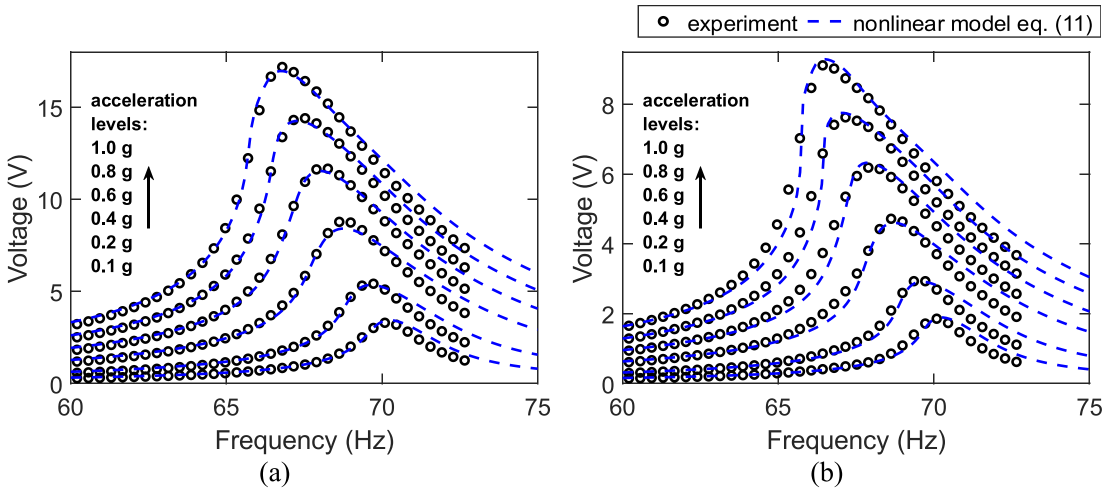

Figure 5. Comparison of experimental voltage response with model at $R = 10$ MΩ: (a) PZT5H series (b) PZT5H parallel. Arrow indicates the direction of increasing acceleration level.

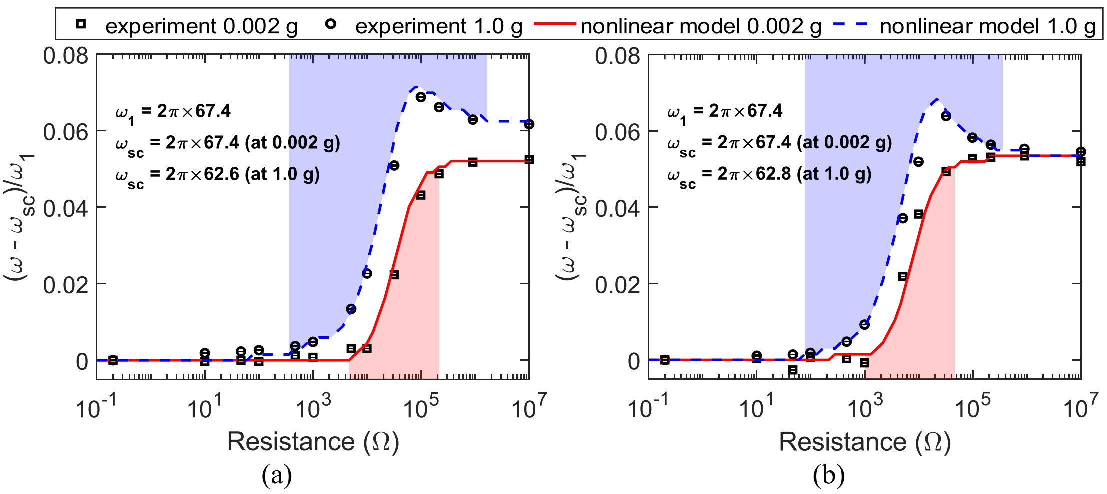

Figure 6. Normalized electromechanical frequency shift vs. load resistance: (a) PZT5H series (b) PZT5H parallel. Shaded areas indicate the transition region from ω_{sc} to ω_{oc}.

3.4. Effect of load resistance on electromechanical performance

In this section, we examine the resonance frequency, tip displacement, and power output across a range of load resistances from 0 Ω to 10 MΩ, comparing experimental and numerical data. For each load resistance, the resonance frequency, tip displacement, and power output at resonance are recorded and analyzed at both low and high acceleration levels. The effects of damping assumptions on numerical predictions of tip displacement and power output are investigated.

3.4.1. Resonance frequency

Figure 6 analyzes the normalized electromechanical frequency shift, expressed as $(\omega - \omega_{sc})/\omega_1$, for two base acceleration levels: 0.002 g (linear case) and 1.0 g (nonlinear case). Here, ω is the resonance frequency at a given resistance R, while ω_{sc} is the short-circuit resonance frequency. The difference between them is normalized using the first natural frequency ω_1 to facilitate a clear comparison between linear and nonlinear cases. The error bars of the experimental data are also included in figure 6, however, the errors are very small and therefore not clearly visible. These errors arise from measurement sensitivity limits as well as repeatability and systematic variations across identical samples.

In the linear case, resonance frequency remains constant at the short-circuit value ω_{sc} until a critical transition region where it rapidly increases, thereafter settles at the open-circuit value ω_{oc}.

In the nonlinear case, the linear model is inadequate for predicting the resonance frequency behavior. The transition region begins at a load resistance an order of magnitude smaller than that in the

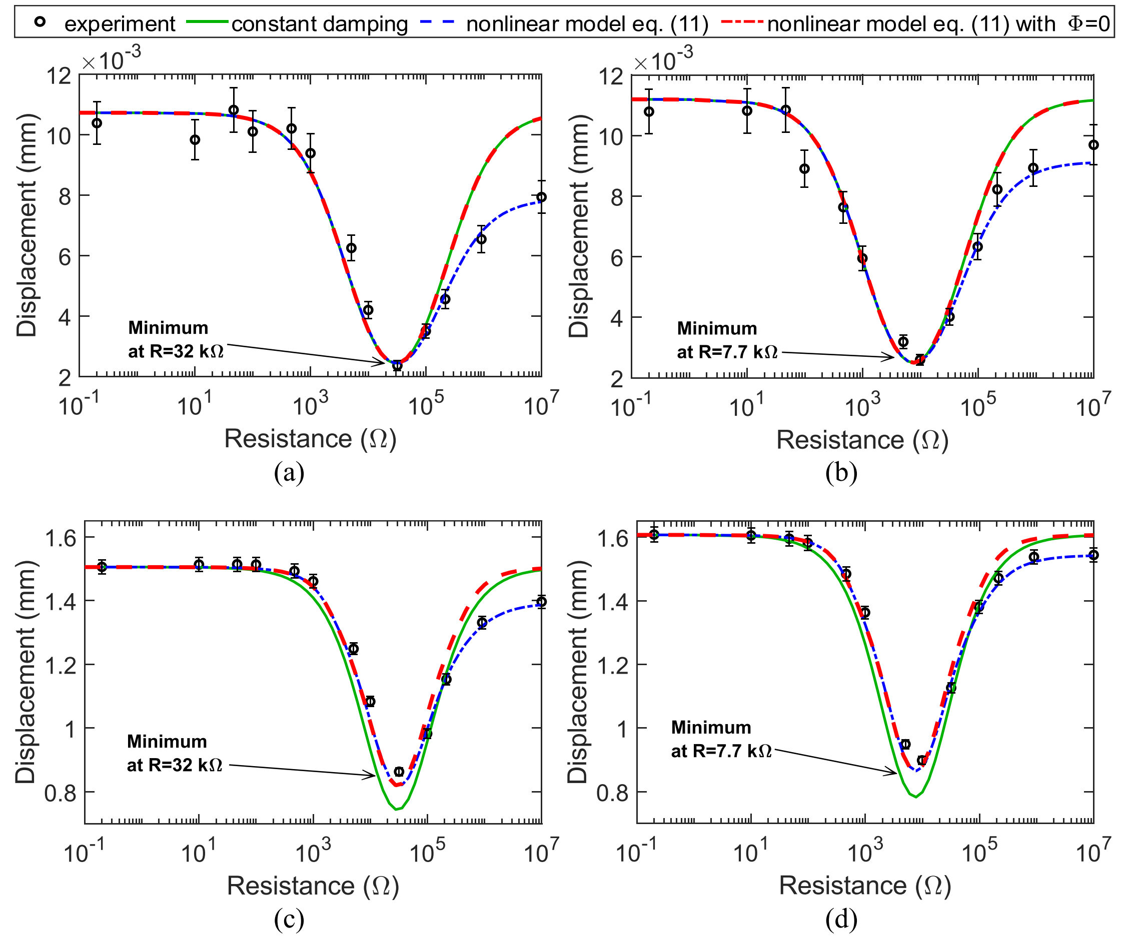

Figure 7. Tip displacement vs. load resistance: (a) PZT5H series at 0.002 g. (b) PZT5H parallel at 0.002 g (c) PZT5H series at 1.0 g (d) PZT5H parallel at 1.0 g.

linear case, due to nonlinearity's softening effect. The resonance frequency peaks before settling to the open-circuit value, unlike the simple leveling off observed in linear cases. This peak results from the competing effects of elastic nonlinearity, which lowers the resonance frequency, and electromechanical coupling, which raises it. Electromechanical energy conversion increases the resonance frequency through a stiffening effect in the transition region. However, as this conversion decreases towards the end of the region, the softening effect of elastic nonlinearity becomes stronger and reduces the resonance frequency. The nonlinear model from equation (11) predicts this behavior well for both samples.

3.4.2. Tip displacement

Figure 7 shows the evolution of peak tip displacement observed during the experimental frequency sweep for various load resistances ranging from 0 Ω to 10 MΩ. Three numerical curves are shown alongside experimental data: one assuming constant damping within the nonlinear model, another using the nonlinear model from equation (11) with damping parameters listed in table 3, and a third using the same nonlinear model with dielectric dissipation set to zero. For the constant damping assumption, the equivalent damping is calculated at the respective base acceleration level in short-circuit and kept constant across all load resistances, similar to the method used by Patel *et al* [21].

Error bars for the experimental data are also included in figure 7. Larger errors are observed at low acceleration levels because the displacement and voltage amplitudes are small, making them more sensitive to measurement accuracy and experimental noise.

The critical load resistance is defined as any load resistance value at which a local extremum (maximum or minimum) occurs in the system's peak response amplitude as the load resistance is varied.

As the load resistance increases, the peak tip displacement initially remains nearly constant, then decreases to a minimum at a critical load resistance, and subsequently increases until it stabilizes. The critical load resistances are 32 kΩ for the PZT5H series and 7.7 kΩ for PZT5H parallel, that we tested.

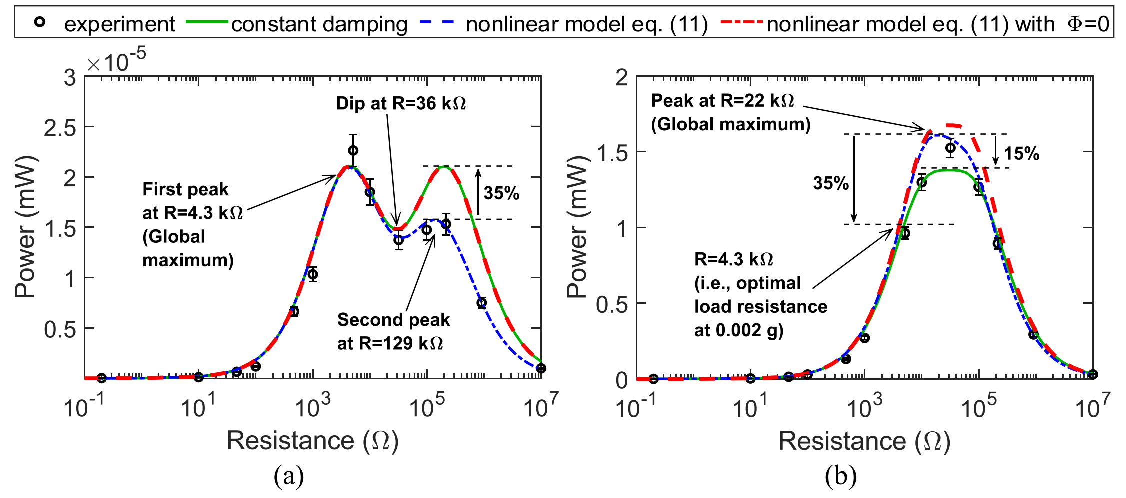

Figure 8. Power vs. load resistance: (a) PZT5H series at 0.002 *g* (b) PZT5H series at 1.0 *g*.

The critical load resistance for parallel configuration is smaller than that of series configuration due to its larger capacitance.

As shown in figure 7, the nonlinear model based on equation (11) shows good agreement with the experimental tip displacement across a broad range of load resistances, whereas models based on simplified damping assumptions exhibit noticeable deviation.

The constant damping within the nonlinear model uses the same methodology for calculating the response as described in our previously developed unified nonlinear model in [36]. Under the constant damping assumption, the model agrees well with experimental data at low acceleration levels and for low to moderate load resistances, where nonlinear structural dissipation is negligible due to small vibration amplitudes. However, at higher load resistances, dielectric losses become increasingly significant, resulting in noticeable deviations from experimental observations. At higher acceleration levels, this model captures the response accurately only at low load resistances, where the tip displacement approaches its short-circuit value. To match the experimental data, the model based on constant damping assumption requires recalculation of the damping parameter at each load resistance value. This makes the model calculations very cumbersome and limits the accuracy. In contrast, the proposed advanced nonlinear model in the current work captures the full evolution of tip displacement across varying load resistances and excitation levels, demonstrating improved predictive capability.

The curve resulting from assuming zero dielectric dissipation Φ in equation (11), while keeping other parameters the same as table 3, aligns with experimental data around resistances smaller than or equal to the critical load resistance. The contribution of Φ is voltage-dependent, as indicated in equation (9). Thus, its effect becomes more significant at larger resistances where higher voltages are observed.

3.4.3. Power output

Figure 8 presents the corresponding evolution of peak power output, calculated as $|V|^2/R$, during the experimental frequency sweep. The experimental results are compared with three numerical curves, as described in section 3.4.2, which are: assuming constant damping within the nonlinear model, the nonlinear model from equation (11) with damping parameters from table 3, and the same nonlinear model with dielectric dissipation neglected.

At a low acceleration of 0.002 *g*, as shown in figure 8(a), the power output displays two peaks with a dip between them, indicative of systems with strong electromechanical coupling and low damping [33, 39, 41]. We identify three critical load resistances: 4.3 kΩ where the power output is highest; 36 kΩ which corresponds to a dip; and 129 kΩ marking another peak. The resonance frequencies associated with the load resistances at the power output peaks correspond to the short-circuit and open-circuit resonance frequencies, as observed in figure 6(a). The power output behavior differs from that of the tip displacement, which shows a single minimum at 31 kΩ, as shown in figure 7. Notably, the power output dip roughly aligns with this minimum in tip displacement. The measurement error is larger at this

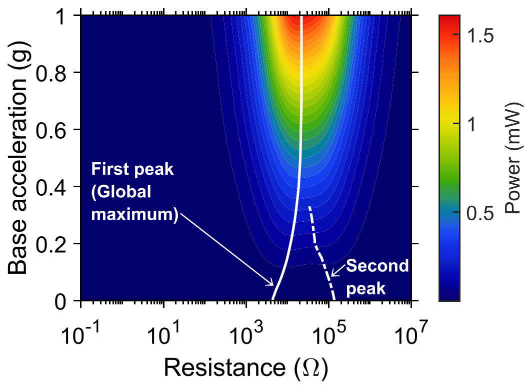

Figure 9. Analytical power output vs. base acceleration and load resistance for PZT5H series.

low acceleration level (approximately 7%), which is reasonable given the noisy experimental environment at small vibration amplitudes. These voltage measurement errors further propagate and amplify during the power calculation. Nonetheless, the numerical power calculated through nonlinear model is mostly within the error bounds of experimental data.

As acceleration increases, the range of critical load resistances becomes narrower due to nonlinear structural dissipation that preferentially attenuates the response near short-circuit and open-circuit resonance frequencies [33]. At an acceleration level of 1.0 g, only one peak is observed at 22 kΩ, as shown in figure 8(b).

The nonlinear model of equation (11) shows a strong correlation with the experimental data, as illustrated in figure 8, capturing key trends more effectively than models employing simplified damping assumptions.

The assumption of constant damping appears to underestimate the power output by 15% when approaching critical load resistance at higher acceleration levels as shown in figure 8(b). The assumption of negligible dielectric dissipation (i.e. $\Phi = 0$) in equation (11) results in a 35% overestimation of power output around the second peak at lower acceleration levels as shown in figure 8(a).

We define the load resistance at the global power output maximum as the optimal load resistance, while resistances associated with peaks (local maxima) or dip (local minima) are termed critical load resistances as described previously. The optimal load resistance for PZT5H series is 4.3 kΩ at 0.002 g and 22 kΩ at 1.0 g.

In figure 9, we examine the analytical power output across various base accelerations and load resistances to determine the optimal load resistance for energy harvesting. As acceleration increases, the spread of critical load resistances narrows, and the optimal load resistance increases and eventually levels off. A critical acceleration threshold is identified at 0.3 g for the bimorph-series PEH, beyond which the two power output peaks merge into one, and the second peak becomes indistinct.

Figure 10(a) compares the critical load resistance for power output peaks with the critical load resistance observed for minimum tip displacement. The resonance frequencies associated with these critical load resistances, termed critical resonance frequencies, are examined in figure 10(b). While the optimal load resistance for power output increases and levels off with acceleration, the critical load resistance for minimum tip displacement remains unchanged. Critical resonance frequency decreases with increasing acceleration due to material nonlinearities, with the resonance frequency for the first peak of power output notably lower than that for minimum tip displacement. Furthermore, the narrowing spread of critical resonance frequencies at higher accelerations suggests a reduced operating bandwidth at high acceleration levels.

These results highlight the importance of accurately modeling material nonlinearities and damping to reliably predict the optimal load resistance and resonance frequency for PEHs. Inaccurate assumptions can lead to significant reduction of harvested power output. For instance, as shown in figure 8(b), operating the harvester at an acceleration of 1.0 g with a load resistance of 4.3 kΩ (corresponding to the optimal resistance at 0.002 g) results in a power output approximately 35% lower than the maximum achievable value at the correct optimal load resistance for that acceleration level.

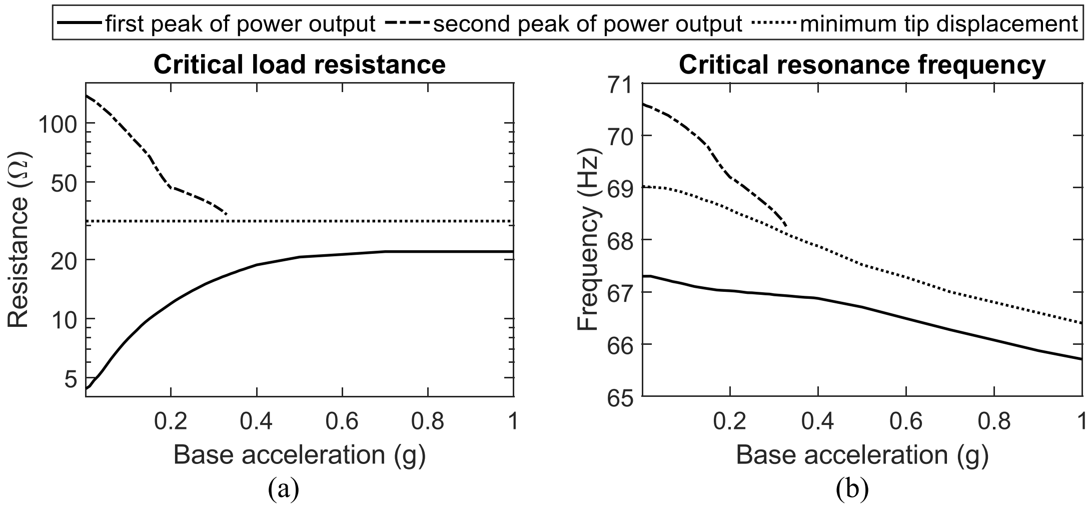

Figure 10. (a) Critical load resistance (b) critical resonance frequency for PZT5H series.

4. Conclusion

This research presents an advanced nonlinear model for PEHs, incorporating elastic, electromechanical coupling, and damping nonlinearities. It accurately models structural dissipation, electromechanical conversion losses, and dielectric losses. Experimental results from two PEH samples are used for comparison with the model (bimorph-series and bimorph-parallel). The PEH is excited at high base acceleration levels that induce strains in the piezoelectric material close to its maximum operable strain limit, enabling characterization of the associated nonlinearity coefficients and damping parameters under high-strain conditions. Through an analytical approach, the model successfully determines these parameters. Elastic nonlinearity leads to a softening behavior, whereas the electromechanical coupling nonlinearity leads to a stiffening effect, especially at high acceleration levels. The previously developed nonlinear models with constant damping could only match experiments over a limited range of load resistances and required recalculating damping at each resistance value, making it impractical and less accurate. In contrast, the advanced nonlinear model developed in this work overcomes these limitations and accurately predicts resonance frequency, displacement, and power output across wide range of acceleration levels and load resistances. The current model shows much closer agreement with experimental data than previous nonlinear models.

Nonlinear structural dissipation and dielectric losses have a significant impact near the optimal load resistance. The optimal load resistance for energy harvesters increases with acceleration level and eventually levels off while the corresponding resonance frequency decreases throughout. Incorrect modeling assumptions can result in a design with much lower power output than its maximum potential. It is essential to incorporate material nonlinearities, nonlinear structural dissipation, and dielectric losses into the model for the optimal design of PEHs.

Data availability statement

All data that support the findings of this study are included within the article (and any supplementary files).

Acknowledgments

The authors kindly acknowledge Bell Textron Canada Ltd for their support and funding of this research through the Industry Canada Technology Demonstration Program (TDP) and the MITACS program.

Conflict of interest

The author(s) declared no conflicts of interest with respect to the research, authorship, and/or publication of this article.

Appendix

The time dependence is expanded in multiple scales as $T_k = \epsilon^k t$ where ε is a small bookkeeping parameter [39]. The time derivatives are defined as

$$\frac{\mathrm{d}}{\mathrm{d}t} = \mathrm{D}_0 + \varepsilon \mathrm{D}_1 + \varepsilon^2 \mathrm{D}_2 \tag{A.1}$$

$$\frac{\mathrm{d}^2}{\mathrm{d}t^2} = \mathrm{D}_0^2 + 2\varepsilon \mathrm{D}_0\mathrm{D}_1 + \varepsilon^2 \mathrm{D}_1^2 + 2\varepsilon^2 \mathrm{D}_0\mathrm{D}_2 \tag{A.2}$$

where $\mathrm{D}_k = \partial/\partial T_k$.

The tip displacement and voltage can also be expanded in multiple scales as,

$$\eta_1(t) = \eta_{10} + \varepsilon\eta_{11} + \varepsilon^2\eta_{12}; \quad V_1(t) = V_{10} + \varepsilon V_{11} + \varepsilon^2 V_{12}. \tag{A.3}$$

We balance all linear coefficients at the zeroth-order perturbation correction (ε^0), except the electromechanical coupling and forcing terms, which are scaled to higher order similar to the method described in [22, 24]. The second-order nonlinearities may be scaled to ε^1, but their coefficients reduce to zero due to cantilever symmetry. Therefore, they are omitted from the perturbation solution derivation to simplify the equations. The coefficients associated with dissipation and higher-order nonlinear coefficients in the governing equations are scaled with ε^2. Based on preliminary comparison with the time-domain numerical solution, higher-order perturbation corrections were found unnecessary. Accordingly, the coefficients are scaled only up to ε^2.

Material nonlinearities and structural damping are scaled with ε^2, while the remaining terms are of order ε^0 [22].

Substituting equations (A.1)–(A.3) in equations (9) and (10), and assembling the coefficients of ε^0 gives

$$\mathrm{D}_0^2\eta_{10} + \omega_1^2\eta_{10} = 0 \tag{A.4}$$

$$C\mathrm{D}_0 V_{10} + \Theta \mathrm{D}_0\eta_{10} + \frac{V_{10}}{R} + \Lambda \mathrm{D}_0^2\eta_{10} + \Phi\, \mathrm{D}_0^2 V_{10} = 0. \tag{A.5}$$

Similarly, assembling the coefficients of ε^1 gives

$$\mathrm{D}_0^2\eta_{11} + 2\mathrm{D}_0\mathrm{D}_1\eta_{10} + \omega_1^2\eta_{11} = 0 \tag{A.6}$$

$$C\mathrm{D}_0 V_{11} + C\mathrm{D}_1 V_{10} + \Theta \mathrm{D}_0\eta_{11} + \Theta \mathrm{D}_1\eta_{10} + \frac{V_{11}}{R} + \Lambda \mathrm{D}_0^2\eta_{11} + 2\Lambda \mathrm{D}_0\mathrm{D}_1\eta_{10} + \Phi\, D_0^2 V_{11} + 2\Phi\, \mathrm{D}_0\mathrm{D}_1 V_{10} = 0. \tag{A.7}$$

Similarly, assembling the coefficients of ε^2 gives

$$\begin{aligned} &\mathrm{D}_0^2\eta_{12} + 2\mathrm{D}_0\mathrm{D}_1\eta_{11} + \mathrm{D}_1^2\eta_{10} + 2\mathrm{D}_0\mathrm{D}_2\eta_{10} + B\mathrm{D}_0\eta_{10} + \sum_{k=1}^{n-1} G_{\mathrm{m},k}\eta_{10}^k \mathrm{D}_0\eta_{10} \\ &- \Lambda \mathrm{D}_0 V_{10} + \omega_1^2\eta_{12} + \sum_{k=2}^{n-1} N_{\mathrm{m},k}\eta_{10}^{k+1} - \Theta V_{10} - \sum_{k=2}^{n-1} N_{\mathrm{e},k}\eta_{10}^k V_{10} = \Gamma\,|\ddot{v}_\mathrm{b}|\cos(\Omega t) \end{aligned} \tag{A.8}$$

$$\begin{aligned} &C\mathrm{D}_0 V_{12} + C\mathrm{D}_1 V_{11} + C\mathrm{D}_2 V_{10} + \Theta \mathrm{D}_0\eta_{12} + \Theta \mathrm{D}_1\eta_{11} + \Theta \mathrm{D}_2\eta_{10} \\ &+ \sum_{k=2}^{n-1} N_{\mathrm{e},k}\eta_{10}^k \mathrm{D}_0\eta_{10} + \tfrac{V_{12}}{R} + \Lambda \mathrm{D}_0^2\eta_{12} + 2\Lambda \mathrm{D}_0\mathrm{D}_1\eta_{11} + \Lambda \mathrm{D}_1^2\eta_{10} + 2\Lambda \mathrm{D}_0\mathrm{D}_2\eta_{10} + \Phi\, \mathrm{D}_0^2 V_{12}\ . \\ &+ 2\Phi\, \mathrm{D}_0\mathrm{D}_1 V_{11} + \Phi\, \mathrm{D}_1^2 V_{10} + 2\Phi\, \mathrm{D}_0\mathrm{D}_2 V_{10} = 0 \end{aligned} \tag{A.9}$$

The solution to the first-order equations (A.4) and (A.5) is given by

$$\eta_{10} = P(T_1, T_2)\, e^{i\omega_1 T_0} + \text{c.c.}; \quad V_{10} = Q(T_1, T_2)\, e^{i\omega_1 T_0} + \text{c.c.} \tag{A.10}$$

where 'c.c.' denotes the complex conjugate of the preceding terms, and this notation is used throughout the article to indicate the same. Here, P is the generalized vibration response function, and Q is the voltage response function, both of which are complex-valued functions of T_1 and T_2. The voltage response function and generalized vibration response function are related as $Q = ZP$, where Z is a complex-value electromechanical conversion factor expressed as $Z = \frac{-i\omega_1\Theta+\omega_1^2\Lambda}{i\omega_1 C+1/R-\omega_1^2\Phi}$.

By substituting the first-order solution into equation (A.6) and removing the secular terms (i.e. $\sim e^{i\omega_1 T_0}$) [39], the resulting condition is $D_1 P = 0$ which implies that P is a function of T_2 and is independent of T_1 Thus, the polar form of the generalized vibration response function P is written as $P = \frac{1}{2}pe^{i\psi}$, where P is the generalized vibration response amplitude and ψ is its argument, both of which are real functions of T_2.

This polar representation is employed, and the solution from equation (A.6) is substituted into equation (A.8). Secular terms (i.e. $\sim e^{i\omega_1 T_0}$) in the resulting expression are then removed, followed by separation into real and imaginary parts as shown below

$$\omega_1 p' + \frac{B}{2}\omega_1 p + \omega_1 J_\mathrm{m} - \frac{\Lambda}{2}\omega_1 Z_\mathrm{Re} p - \frac{1}{2}\Theta Z_\mathrm{Im} p - Z_\mathrm{Im} S_\mathrm{e} = \Gamma\frac{|\ddot{v}_\mathrm{b}|}{2}\sin(\sigma T_2 - \psi) \tag{A.11}$$

$$-\omega_1 \psi' p + \frac{\Lambda}{2}\omega_1 Z_\mathrm{Im} p + S_\mathrm{m} - \frac{1}{2}\Theta Z_\mathrm{Re} p - Z_\mathrm{Re} S_\mathrm{e} = \Gamma\frac{|\ddot{v}_\mathrm{b}|}{2}\cos(\sigma T_2 - \psi). \tag{A.12}$$

In the above equations, $\frac{\mathrm{d}p}{\mathrm{d}T_2}$ and $\frac{\mathrm{d}(\sigma T_2-\psi)}{\mathrm{d}T_2}$ are considered zero under steady-state conditions. Equations (A.11) and (A.12) are then squared, summed, and solved for σ leading to equation (11).

ORCID iDs

Radhika Choudhary 0000-0003-3188-4032
Edith Roland Fotsing 0000-0002-0967-9094
Annie Ross 0000-0002-3767-6958
Guilhem Michon 0000-0003-0747-7680

References

[1] Hashim A A, Mahmoud K I and Ridha H M 2021 Geometry and shape optimization of piezoelectric cantilever energy harvester using COMSOL multiphysics software *Int. Rev. Appl. Sci. Eng.* **12** 103–10
[2] Basari A A *et al* 2014 Shape effect of piezoelectric energy harvester on vibration power generation *J. Power Energy Eng.* **02** 117–24
[3] Ben Ayed S, Abdelkefi A, Najar F and Hajj M R 2014 Design and performance of variable-shaped piezoelectric energy harvesters *J. Intell. Mater. Syst. Struct.* **25** 174–86
[4] Goldschmidtboeing F and Woias P 2008 Characterization of different beam shapes for piezoelectric energy harvesting *J. Micromech. Microeng.* **18** 104013
[5] Dietl J M and Garcia E 2010 Beam shape optimization for power harvesting *J. Intell. Mater. Syst. Struct.* **21** 633–46
[6] Sarafraz A A and Seyed Roknizadeh S A 2017 Shape and geometrical parameter effects of a bimorph piezoelectric beam on energy harvesting performance *J. Appl. Comput. Mech.* **3** 92–102
[7] Gao X, Shih W-H and Shih W Y 2009 Induced voltage of piezoelectric unimorph cantilevers of different nonpiezoelectric/piezoelectric length ratios *Smart Mater. Struct.* **18** 125018
[8] Friswell M I and Adhikari S 2010 Sensor shape design for piezoelectric cantilever beams to harvest vibration energy *J. Appl. Phys.* **108** 014901
[9] Shu Y C and Lien I C 2006 Analysis of power output for piezoelectric energy harvesting systems *Smart Mater. Struct.* **15** 1499–512
[10] Ajitsaria J, Choe S Y, Shen D and Kim D J 2007 Modeling and analysis of a bimorph piezoelectric cantilever beam for voltage generation *Smart Mater. Struct.* **16** 447–54
[11] Guyomar D, Aurelle N and Eyraud L 1997 Piezoelectric ceramics nonlinear behavior. Application to Langevin transducer *J. Phys. III* **7** 1197–208
[12] Joshi S P 1992 Non-linear constitutive relations for piezoceramic materials *Smart Mater. Struct.* **1** 80–83
[13] von Wagner U and Hagedorn P 2002 Piezo-beam systems subjected to weak electric field: experiments and modelling of non-linearities *J. Sound Vib.* **256** 861–72
[14] Aurelle N, Guyomar D, Richard C, Gonnard P and Eyraud L 1996 Nonlinear behavior of an ultrasonic transducer *Ultrasonics* **34** 187–91
[15] Nima Mahmoodi S, Jalili N, Mahmoodi S N and Jalili N 2007 Non-linear vibrations and frequency response analysis of piezoelectrically driven microcantilevers *Int. J. Non-Linear Mech.* **42** 577–87
[16] Mahmoodi S N, Jalili N N and Daqaq M F 2008 Modeling, nonlinear dynamics, and identification of a piezoelectrically actuated microcantilever sensor *IEEE/ASME Trans. Mechatronics* **13** 58–65
[17] Mahmoodi S N, Daqaq M F and Jalili N 2009 On the nonlinear-flexural response of piezoelectrically driven microcantilever sensors *Sens. Actuators A* **153** 171–9
[18] Choudhary R, Rzig I, Fotsing E R and Ross A 2022 Investigation of the effect of piezoelectric material nonlinearity on unimorph energy harvester *Proc. Int. Congress on Sound and Vibration* (available at: www.scopus.com/inward/record.url?eid=2-s2.0-85149888836&partnerID=MN8TOARS)
[19] Choudhary R, Rzig I, Fotsing E R and Ross A 2023 Investigation of the electromechanical coupling nonlinearity in piezoelectric energy harvester *Proc. Int. Congress on Sound and Vibration* (available at: www.scopus.com/inward/record.url?eid=2-s2.0-85170639167&partnerID=MN8TOARS)
[20] Priya S, Viehland D, Carazo A V, Ryu J and Uchino K 2001 High-power resonant measurements of piezoelectric materials: importance of elastic nonlinearities *J. Appl. Phys.* **90** 1469–79

[21] Patel R, McWilliam S and Popov A A 2014 Optimization of piezoelectric cantilever energy harvesters including non-linear effects *Smart Mater. Struct.* **23** 085002
[22] Salmani H and Rahimi G H 2018 Study the effect of tapering on the nonlinear behavior of an exponentially varying width piezoelectric energy harvester *Trans. ASME. J. Vib. Acoust.* **140** 1–14
[23] Stanton S C, Erturk A, Mann B P and Inman D J 2010 Nonlinear piezoelectricity in electroelastic energy harvesters: modeling and experimental identification *J. Appl. Phys.* **108** 74903
[24] Stanton S C, Erturk A, Mann B P, Dowell E H and Inman D J 2012 Nonlinear nonconservative behavior and modeling of piezoelectric energy harvesters including proof mass effects *J. Intell. Mater. Syst. Struct.* **23** 183–99
[25] Abdelkefi A, Nayfeh A H and Hajj M R 2012 Effects of nonlinear piezoelectric coupling on energy harvesters under direct excitation *Nonlinear Dyn.* **67** 1221–32
[26] Abdelkefi A, Nayfeh A H and Hajj M R 2012 Global nonlinear distributed-parameter model of parametrically excited piezoelectric energy harvesters *Nonlinear Dyn.* **67** 1147–60
[27] Leadenham S and Erturk A 2015 Unified nonlinear electroelastic dynamics of a bimorph piezoelectric cantilever for energy harvesting, sensing, and actuation *Nonlinear Dyn.* **79** 1727–43
[28] Yang Y and Upadrashta D 2016 Modeling of geometric, material and damping nonlinearities in piezoelectric energy harvesters *Nonlinear Dyn.* **84** 2487–504
[29] Erturk A and Inman D J 2008 A distributed parameter electromechanical model for cantilevered piezoelectric energy harvesters *Trans. ASME. J. Vib. Acoust.* **130** 1–15
[30] Patel R, McWilliam S and Popov A A 2011 A geometric parameter study of piezoelectric coverage on a rectangular cantilever energy harvester *Smart Mater. Struct.* **20** 085004
[31] Bae S and Kim P 2021 Load resistance optimization of a broadband bistable piezoelectric energy harvester for primary harmonic and subharmonic behaviors *Sustainability* **13** 2865
[32] Choudhary R, Rzig I, Fotsing E R and Ross A 2024 Parametric investigation of energy harvester design—piezoelectric coverage and cantilever length *Proc. Int. Congress on Sound and Vibration* (available at: www.scopus.com/record/display.uri?eid=2-s2.0-85205361910&origin=inward&txGid=d99e222ab77121bd4a61e11d59818095)
[33] Leadenham S and Erturk A 2020 Mechanically and electrically nonlinear non-ideal piezoelectric energy harvesting framework with experimental validations *Nonlinear Dyn.* **99** 625–41
[34] Lan C, Qian F, Liao Y and Zuo L 2022 Power characteristics of vibration-based piezoelectric energy harvesters: the effect of piezoelectric material nonlinearity *Smart Mater. Struct.* **31** 105017
[35] Machado S P, Febbo M, Gatti C D and Osinaga S M 2020 A piezoelectric beam model with geometric, material and damping nonlinearities for energy harvesting *Smart Mater. Struct.* **29** 095009
[36] Choudhary R, Rzig I, Fotsing E R and Ross A 2025 A unified nonlinear model of piezoelectric cantilever beams with complex geometries for energy harvesting applications *Smart Mater. Struct.* **34** 025010
[37] Nayfeh A H 2000 *Perturbation Methods* (Wiley) (https://doi.org/10.1002/9783527617609)
[38] Masana R and Daqaq M F 2011 Electromechanical modeling and nonlinear analysis of axially loaded energy harvesters *Trans. ASME. J. Vib. Acoust.* **133** 1413–20
[39] Erturk A and Inman D J 2011 *Piezoelectric Energy Harvesting* (Wiley) (https://doi.org/10.1002/9781119991151)
[40] Daqaq M F, Stabler C, Qaroush Y and Seuaciuc-Osório T 2009 Investigation of power harvesting via parametric excitations *J. Intell. Mater. Syst. Struct.* **20** 545–57
[41] Priya S and Inman D J 2009 *Energy Harvesting Technologies* vol 1 (Springer)